Active transport on disordered microtubule networks: The generalized random velocity model

Aviv Kahana,[1,2] Gilad Kenan,[1] Mario Feingold,[2] Michael Elbaum,[3] and Rony Granek[1,4,*]
[1]*Department of Biotechnology Engineering, Ben-Gurion University of The Negev, Beer Sheva 84105, Israel*
[2]*Department of Physics, Ben-Gurion University of The Negev, Beer Sheva 84105, Israel*
[3]*Department of Materials and Interfaces, The Weizmann Institute of Science, Rehovot 76100, Israel*
[4]*The Ilse Katz Center for Meso and Nanoscale Science and Technology and the Reimund Stadler Minerva Center for Mesoscale Macromolecular Engineering, Ben-Gurion University of The Negev, Beer Sheva 84105, Israel*
(Received 3 July 2008; published 13 November 2008)

The motion of small cargo particles on microtubules by means of motor proteins in disordered microtubule networks is investigated theoretically using both analytical tools and computer simulations. Different network topologies in two and three dimensions are considered, one of which has been recently studied experimentally by Salman *et al.* [Biophys. J. **89**, 2134 (2005)]. A generalization of the random velocity model is used to derive the mean-square displacement of the cargo particle. We find that all cases belong to the class of anomalous superdiffusion, which is sensitive mainly to the dimensionality of the network and only marginally to its topology. Yet in three dimensions the motion is very close to simple diffusion, with sublogarithmic corrections that depend on the network topology. When details of the thermal diffusion in the bulk solution are included, no significant change to the asymptotic time behavior is found. However, a small asymmetry in the mean microtubule polarity affects the corresponding long-time behavior. We also study a three-dimensional model of the microtubule network in living animal cells. Three first-passage-time problems of intracellular transport are simulated and analyzed for different motor processivities: (i) cargo that originates near the nucleus and has to reach the membrane, (ii) cargo that originates from the membrane and has to reach the nucleus, and (iii) cargo that leaves the nucleus and has to reach a specific target in the cytoplasm. We conclude that while a higher motor processivity increases the transport efficiency in cases (i) and (ii), in case (iii) it has the opposite effect. We conjecture that the balance between the different network tasks, as manifested in cases (i) and (ii) versus case (iii), may be the reason for the evolutionary choice of a finite motor processivity.

DOI: 10.1103/PhysRevE.78.051912 PACS number(s): 87.16.Wd, 87.16.Uv, 87.16.Nn, 05.40.−a

I. INTRODUCTION

The genetic content of a living cell is predetermined and complete from its inception. Yet additional mechanisms are required to translate the program into morphology [1]. This role falls largely to the cytoskeleton and to its associated "motor proteins" [2–4]. The cytoskeleton consists of three distinct, even though interconnected, networks of protein filaments: microtubules, filamentous actin (F-actin), and several families of intermediate filaments. Microtubules and F-actin are associated with motor proteins: kinesin and dynein for the former and myosin for the latter. Due to structural asymmetry in the filaments, the motors are able to sense their directionality. Dynein motors move exclusively from plus to minus ends of microtubules, while most kinesin forms move from minus to plus [3,4]. Most myosins move from the pointed end toward the barbed end of actin filaments.

The microtubule network spans through the whole cell. This makes it ideally suited for delivery of cargos—e.g., vesicles, organelles, or mRNA—from the membrane to the nucleus and vice versa or from the membrane and nucleus to different cell compartments—e.g., the ribosome. Recently, it has been shown that various animal viruses—e.g., adenoviruses, the Herpes Simplex virus, and the HIV—take advantage of microtubule-based transport for delivery to the nuclear envelope, where the genome is released through nuclear pores [5–9]. Theoretical studies of active transport in microtubule networks may shed light on the efficiency of such processes, but only a few studies have been presented so far [10].

Several experimental approaches have been developed to evaluate motor function. These include single-molecule imaging studies [11–13], bead-based assays [15–17], and force transducers based on optical tweezers [18–22]. Recently, motor-assisted transport along microtubules of a protein-DNA complex containing a nuclear localization signal has been experimentally studied *in vitro* [13]. The system is based on a cell-free Xenopus egg extract [14]. Direct single-particle tracking and detailed statistical analysis have been used to deduce the mean-square displacement (MSD) and probability distribution function (PDF). A disordered three-dimensional (3D), plane-oriented, microtubule network forms in the sample. The microtubules are mainly oriented in the (x,y) plane; however, since the thickness of the sample is significantly larger than the mesh size, there are several layers of microtubules along the z axis. The observed MSD of the cargo in the (x,y) plane is found to behave similarly to that of a Brownian particle, increasing linearly with time, even though chemical and antibody inhibition studies clearly show that the transport is of active nature and is based primarily on dynein. It is therefore important to understand the way that active transport in such a disordered microtubule network leads to diffusivelike transport. Moreover, *in vitro* networks may be created in other topologies and the connec-

*Author to whom correspondence should be addressed. rgranek@bgu.ac.il

tion between the topology and the resulting MSD is of general interest. The initial theoretical steps required to explain this behavior have been recently put forward [13]. The active transport involved is similar to transport on a disordered railway track network. On each track only one direction of motion is allowed. The "locomotor" moves with constant velocity on a single track, then falls off and hops to one of the nearest-neighboring tracks and so on.

In intact animal cells, microtubules usually project radially from a centrosome with outward polarity (minus ends at the centrosome). This allows the delivery nuclear-targeted cargo to the nuclear envelope using dynein or membrane-targeted cargo to the membrane using kinesin. Yet cargos that need to reach a localized cell compartment, positioned away from the centrosome and the membrane, will have to follow a more complicated route, involving more than one track. Moreover, due to large internal stresses that induce bending of the microtubules, the network often becomes uniformly disordered on a local scale even if global polarity remains (see Ref. [1], p. 807), suggesting that transport on short length scales may be similar to the transport studied *in vitro* [13]. In fact, living cells are not always organized around a centrosome from which microtubules grow. In some animal cells, the microtubule network is disordered with respect to both the position of microtubules and their polarity [23]. In plant cells, while microtubules do nucleate around the nuclear envelope, there may also be nucleation throughout the cytoplasm.

From a statistical physics viewpoint, motion on a microtubule network is similar to the random velocity model (RVM), where all tracks (the field lines) are parallel to each other [24–26]. In the simplest case, to which we shall refer in the following as the $(1+1)$-dimensional [$(1+1)$D model] the particle performs a 1D random walk between "tracks" with random polarity, leading to a quenched disordered velocity field. The result is enhanced (or "super") diffusion of the particle in the direction parallel to the tracks with an MSD increasing as $\sim t^{3/2}$ [24]. In the corresponding $(2+1)$D model, tracks form a 2D parallel array with randomly assigned polarity. In this case, the resulting enhanced diffusion is more moderate with the MSD increasing as $\sim t \ln t$ [25]. However, in both models tracks do not intersect, whereas, as described above, in realistic microtubule networks intersections are common. A motor protein moving on a microtubule will fall off after a short "processivity time" typically of the order of 1 s, diffuse in the solution, and subsequently attach to an adjacent microtubule whose polarity is uncorrelated to the polarity of the first microtubule. Therefore, application of the random velocity model to transport on microtubule networks requires a suitable generalization of the model. Renormalization group calculations for such "velocity fields" have been carried out and are closely related to the models studied in this paper [27]. Studies concerning motion on a single microtubule track in restricted geometries are also closely related to the present work [28,29]

In what follows we study several models of disordered microtubule networks. Three different network topologies are considered: a purely 2D square lattice network, a purely 3D simple cubic network, and a 3D network that consists of alternating planes of $(1+1)$D organization. The latter models the experimental system studied in Ref. [13]. We show that the resulting enhanced diffusion of the particle is sensitive to both the dimension and topology of the network. In order to model the transport more realistically, in a separate study of a 3D network we include the diffusion in the bulk solution and the falling off and attachment processes between bulk solution and microtubules. As expected, including such details does not affect the scaling behavior in time. We further extend our analysis to asymmetric networks where the global mean polarity does not vanish, leading to a crossover at long times to a partially diffusive behavior. Finally, we present the case of a 3D animal cell model. It mimics a 3D animal cell with microtubules that radiate from a centrosome (also known as a microtubule organization center), ending near the cell membrane. The model includes significant local orientational disorder, on top of the radial global orientation. We examine transport efficiency [30] for three cases: (i) cargo that originates at the nucleus and has to reach the membrane, (ii) cargo that originates at the membrane and has to reach the nucleus, and (iii) cargo that leaves the nucleus and has to reach a specific localized target in the cytoplasm. The transport efficiency is characterized in the three cases via the first-passage-time probability and examined for varying motor processivities. We discuss the role of the finite motor processivity in optimizing the transport for different network tasks.

II. RANDOM VELOCITY MODEL: A REVIEW

Before dealing with realistic microtubule networks, we briefly review the random velocity model for simple topologies that have been analyzed theoretically in the past. The theoretical tools that have been developed to analyze this model will later allow us to analyze realistic microtubule networks.

The symmetric (1+1)D model. The random velocity model [24,26,25,27] was originally introduced for the study of ground water flow in layered media and was defined in 2D [31,32]. In what follows we refer to it as the $(1+1)$D model. It assumes a 1D array of parallel tracks along (say) the y axis. The tracks are assigned random polarities, $+1$ or -1, with equal probabilities—i.e., $p=0.5$ for each direction. Since these values do not change in time, we have quenched polarity disorder. Particles perform random walks between the tracks along the x axis. When a particle attaches to a certain track, it moves with a velocity $\pm v$ according to its polarity. We seek to characterize the net motion along the y axis in the long-time limit, in particular via the MSD.

As the process is stationary, one may either consider a single particle and perform time averaging or, alternatively, an ensemble of particles, each starting from a randomly chosen track. While the corresponding mean $\langle y(t) \rangle$ vanishes, the MSD $\langle y^2(t) \rangle$ does not. Yet since the track "polarity" field (i.e., the velocity field) is quenched, the motion along the y axis is faster than simple diffusion. The MSD for this model has been derived by Zumofen, Klafter, and Blumen [24]:

$$\langle y^2(t) \rangle = \frac{4v^2\xi}{3(\pi D)^{1/2}} t^{3/2}. \tag{1}$$

Here ξ is the mesh size—i.e., the spacing between tracks—and D is the diffusion coefficient of particles along the x

axis. Transport with an MSD that increases as t^α with $\alpha > 1$ is termed enhanced diffusion or superdiffusion. The $\alpha = 3/2$ exponent in this model can be obtained from a simple scaling argument. "Canceling" of the motion in the y direction does not occur whenever the particle reattaches to the previous track. Hence the track that is most visited will dominate the motion, and this track is the track located at the origin, $x=0$. Consequently, one expects that

$$\langle y^2(t)\rangle \sim P_{0,x}(t) v^2 t^2, \tag{2}$$

where $P_{0,x}(t)$ is the probability of return (within a mesh size ξ) to the origin of the x axis—i.e., $P_{0,x}=\xi P_x(0,t)$, where $P_x(x,t)$ is the PDF along the x axis. Since $P_{0,x}(t)\sim t^{-1/2}$ in 1D, this scaling argument leads to $\langle y(t)^2\rangle \sim t^{3/2}$ or, more precisely, $\langle y^2(t)\rangle \approx (v^2\xi/D^{1/2})t^{3/2}$, which is consistent with Eq. (1).

In fact, from the exact procedure of Zumofen *et al.* [24] one may derive a general result for the RVM that holds independently of the exact nature of the motion along the x axis, as long as it remains a stochastic process. Specifically, in the Laplace transform plane [henceforth $\tilde{f}(u)$ denotes the Laplace transform of $f(t)$],

$$\langle \tilde{y}^2(u)\rangle = \frac{2v^2}{u^2}\tilde{P}_{0,x}(u), \tag{3}$$

which justifies the scaling approach of Eq. (2). We may transform Eq. (3) to the time domain to obtain a differential equation for $\langle y^2(t)\rangle$ by taking the initial conditions to be $\langle y^2(0)\rangle = 0$ and $\frac{d}{dt}\langle y^2(t)\rangle|_{t=0}=0$. The latter condition is expected to be exact for the long-time asymptotic behavior when extrapolated to $t=0$. The differential equation is thus

$$\frac{d^2}{dt^2}\langle y^2(t)\rangle = 2v^2 P_{0,x}(t). \tag{4}$$

For $P_{0,x}(t)=\xi/\sqrt{(4\pi Dt)}$ the solution of Eq. (4) is given by Eq. (1). Equation (4) will be a useful starting point for the analysis of networks.

The (2+1)D symmetric model. Consider a 2D parallel array of tracks directed along the y axis—that is, perpendicular to the (x,z) plane. The cargo particle is performing a 2D random walk between these tracks. To find the MSD along the y axis we only need to replace $P_{0,x}(t)$ in Eq. (4) with the probability of return to the origin of the (x,z) plane, $P_{0,xz}(t)$. For a simple random walk among tracks, $P_{0,xz}(t) = \xi^2/(4\pi Dt)$, and the asymptotic behavior can be obtained from Eq. (3) or (4) [27]:

$$\langle y^2(t)\rangle \simeq \frac{v^2\xi^2}{2\pi D} t \ln\left(\frac{t}{\tau_0}\right). \tag{5}$$

Here $\tau_0=\xi^2/(4D)$ is the hopping time between tracks and has been chosen as the short-time cutoff (i.e., $t=0$ has now shifted to $t=\tau_0$). Note that $\langle y^2(t)\rangle \sim t\ln t$, very close to regular diffusion.

Asymmetric (1+1)D and (2+1)D models. Suppose that we introduce asymmetry in the random walk along the x axis, with probability p for a step to the right and q to the left. The mean position is proportional to time, $\langle x(t)\rangle = (p-q)\frac{\xi}{\tau_0}t$ (where τ_0 is the hopping time, $\tau_0=\xi^2/2D$), while the standard deviation about the mean (i.e., the root of the MSD) is proportional to the square root of time, $\langle (x-\langle x\rangle)^2\rangle^{1/2} = 2\sqrt{pq}\xi\sqrt{\frac{t}{\tau_0}}$. Hence, at long times the probability of return to the origin becomes infinitesimally small and the random walker visits essentially only new tracks. Thus, the motion along the y axis becomes equivalent to a random walk with 50% chance to go up and 50% chance to go down and an effective "hopping time" $\tau_0/|p-q|$. In the (1+1)D model we therefore expect a crossover from the $\sim t^{3/2}$ behavior at "short" times (still much longer than τ_0) to $\sim t$ at long times. More quantitatively, we may define δ as the ratio of the root MSD (the standard deviation) to mean distance traveled, $\delta = \frac{\sqrt{\langle \delta x^2(t)\rangle}}{|\langle x(t)\rangle|} = \frac{2\sqrt{pq}}{|p-q|\sqrt{t/\tau_0}}$, such that when $\delta \gg 1$ the symmetric type behavior applies and when $\delta \ll 1$ one obtains regular diffusion. This defines a crossover time $t^* \simeq (\frac{4pq}{(p-q)^2})\tau_0$, and the MSD is predicted to be

$$\langle y^2(t)\rangle \simeq \begin{cases} \dfrac{4v^2\xi}{3(\pi D)^{1/2}} t^{3/2} & \text{for } t \ll t^*, \\ \dfrac{v^2\xi^2}{2D|p-q|} t & \text{for } t \gg t^*. \end{cases} \tag{6}$$

Similarly, a crossover between a $\sim t\ln t$ and a $\sim t$ behavior is expected for the (2+1)D RVM. Note that the long-time behavior is dramatically altered for arbitrarily small deviations from polarity symmetry—that is, for any nonvanishing $p-q$. In practice, however, the long-time behavior *may not be observed* if this deviation is vanishingly small, since the crossover time itself also diverges as $|p-q|\to 0$.

Computer simulations. Computer simulations of the (1+1)D and (2+1)D models have been performed. Below we concentrate only on the *asymmetric* (1+1)D and *symmetric* (2+1)D cases. We have simulated the motion in a large number of realizations for the polarity disorder and a large number of walks in each realization. After averaging over trajectories, the mean position of the particle along the y axis is found to vanish (as expected by symmetry) and the MSDs along this axis are computed.

In the simulations of the *asymmetric* (1+1)D model, the particle has been given a probability $p=0.505$ to hop to the right and $q=1-p=0.495$ to hop to the left. Figure 1 shows the MSD of the (1+1)D model along the y axis (the track orientation axis) as obtained from averaging over 10^4 particles. The data are fitted to At^α (solid and dashed lines). For intermediate time scales (solid line) we find a superdiffusion exponent $\alpha = 1.499 \pm 0.001$ and a prefactor $A = 1.01 \pm 0.01$, in good agreement with the theoretical values $\alpha=1.5$ and (for this parameter set) $A=1.0638$. For long times (dashed line) the simulations yield $\alpha = 1.01 \pm 0.01$, in good agreement with the theoretical value $\alpha=1$, and $A = 186.6 \pm 0.6$, which is about twice the theoretical value $A=100$. This disagreement is due either to the limited simulation time or to the limitations of the theoretical approach. The crossover time obtained from the simulations is $t^* \sim 8\times 10^3 \tau_0$, in the same range as the theoretical estimate $t^* \sim 10^4\tau_0$.

In the simulations of the *symmetric* (2+1)D model, at each site the particle has probability $f=0.7$ to stay on a track and probability $1-f=0.3$ to hop to one of the four neighbor-

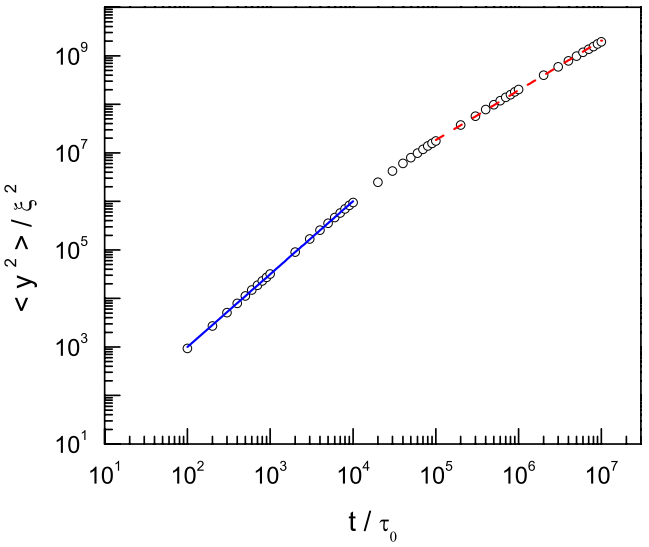

FIG. 1. (Color online) The MSD in the asymmetric (1+1)D RVM, normalized by ξ^2, where ξ is the distance between tracks. The circles are simulation data. The lines are best fits of the data to $\langle y^2 \rangle = At^{\alpha}$. For intermediate time scale (solid line) $A = 1.01 \pm 0.01$ and $\alpha = 1.499 \pm 0.001$; for long time scale (dashed line) $A = 186.6 \pm 0.6$ and $\alpha = 1.003 \pm 0.031$.

ing tracks (with equal probabilities). The MSD along the tracks (the y axis) is shown in Fig. 2 [shown is $\frac{\langle y^2 \rangle}{t}$ against $\ln(\frac{t}{\tau_0})$] and compared to the corresponding best fit to $\langle y^2 \rangle = At[\ln(\frac{t}{\tau_0})]^{\beta}$ with $A = 1.337 \pm 0.002$ and $\beta = 0.934 \pm 0.001$. While the analytical value (noting that t is measured in units of τ_0) $A = 2/\pi = 0.637$ is about half of the one found in simulations, the exponent β is in good agreement with the analytical prediction $\beta = 1$.

III. ACTIVE TRANSPORT ON DISORDERED MICROTUBULE NETWORKS

We now turn to study active transport on disordered microtubule networks that is carried out by the motor proteins

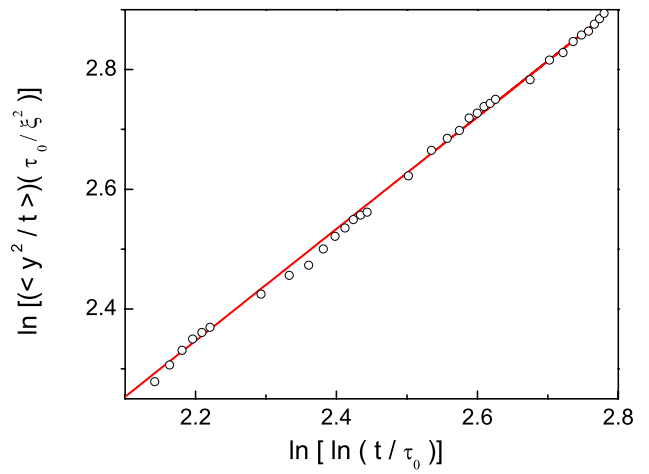

FIG. 2. (Color online) Normalized MSD in the symmetric (2+1)D RVM, divided by the time. The circles are simulation data. The line is a best fit of the data to $\langle y^2 \rangle / t = A[\ln(\frac{t}{\tau_0})]^{\beta}$ with $A = 1.337 \pm 0.002$ and $\beta = 0.934 \pm 0.001$.

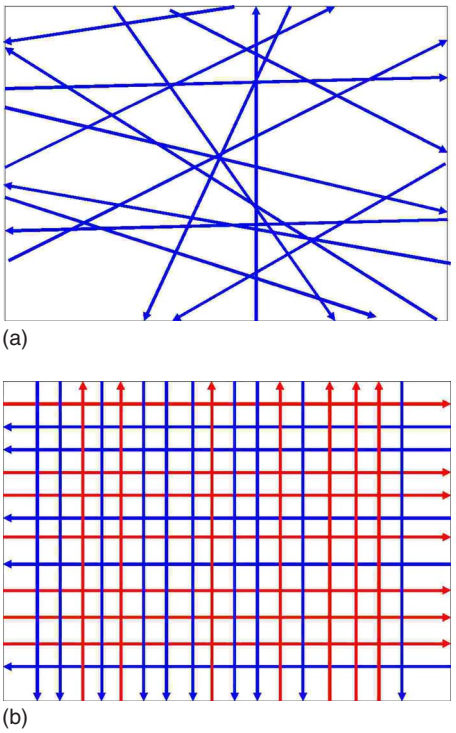

FIG. 3. (Color online) Schematic presentation of 2D microtubule networks. The arrows denote the polarity; i.e., they point towards the minus end of the microtubule. (a) A network with both orientational and polarity disorder. (b) A 2D microtubule, square lattice, network bearing polarity disorder, but no orientational disorder.

kinesin or dynein. We will examine the effect of microtubule polarity disorder in different network topologies in two and three dimensions. The polarity of the microtubule determines the velocity direction of the motor protein (kinesin or dynein) that is attached to it. Therefore, the RVM, generalized here to networks, provides a suitable theoretical framework for the description of such active transport. We will not incorporate into the model the precise orientational disorder that may occur in realistic networks [13], since we believe it will not affect the main characteristics of the transport.

A. Disordered 2D network

First, we consider a purely 2D system, although such systems are hard to realize in experiment. This example will serve as an intermediate case study connecting between the random velocity models discussed in Sec. II and the 3D networks. A disordered 2D network, in which both polarity and orientation are random, is depicted in Fig. 3(a). A simplified version of the model, in which orientational disorder is missing, is shown in Fig. 3(b). Since all microtubules are identical, on average the motion on the network of Fig. 3(b) is isotropic. The same holds for the motion on the network of Fig. 3(a). Moreover, at long times the underlying square lattice in Fig. 3(b) is expected to affect only the fine details and not the main characteristics of the motion. The rationale of this approach is similar to modeling diffusion by using random walk on a lattice, rather than in the continuum.

Let ξ be the mesh size of the network of Fig. 3(b). The particle moves on a particular track with constant velocity v in the direction prescribed by track polarity. At intersections, we assign a probability f for the particle to remain on its track and a probability $1-f$ to hop to the crossing track. In our simulations, f is close to unity (typically above 0.6), allowing the particle to sample many different tracks in the different realizations of the trajectory. Thus, in the limit $1-f \ll 1$ the model corresponds to an exponential processivity waiting time distribution (i.e., the probability of the particle to remain on the track at time t given that it was on the same track at $t=0$) $\Psi(t) \simeq e^{-t/\tau_p}$, where $\tau_p \simeq \tau_v/(1-f)$ and $\tau_v = \xi/v$ is the time it takes to move between two consecutive intersections. For cellular networks the mean processivity time τ_p is typically of order 1 s and v is order 1 μm/s. Thus, for a given mesh size we may determine the model parameter f; e.g., for $\xi \simeq 0.1$ μm we get $f \simeq 0.9$.

Symmetric network. Consider first the case where *exactly* half the tracks are pointing right or left and half up or down. Evaluation of the particle motion characteristics in this system cannot be done using Eq. (4) as for the (1+1)D RVM. Instead, we use a self-consistent approach that is based on the scaling law of Eq. (2) and on the fact that the motion along both axes x and y must be statistically equivalent. Hence, in the long-time limit this motion is described by the two coupled equations

$$\langle y^2(t)\rangle \sim P_{0,x}(t) v^2 t^2, \tag{7}$$

$$\langle x^2(t)\rangle \sim P_{0,y}(t) v^2 t^2. \tag{8}$$

In addition, we assume the following scaling relations between the return probabilities and the corresponding MSDs:

$$P_{0,x}(t) \sim \frac{\xi}{\sqrt{\langle x^2(t)\rangle}} \tag{9}$$

and

$$P_{0,y}(t) \sim \frac{\xi}{\sqrt{\langle y^2(t)\rangle}}. \tag{10}$$

Such relations hold for Gaussian and "stretched-Gaussian" PDFs:

$$P(x,t) = \frac{\gamma}{\Gamma\left(\frac{1}{2\gamma}\right)\sqrt{2\langle x^2(t)\rangle}} \exp\left[-\left(\frac{x^2}{2\langle x^2(t)\rangle}\right)^{\gamma}\right], \tag{11}$$

with $\gamma > 0$ ($\gamma=1$ defines the Gaussian distribution). Since symmetry requires $\langle x^2(t)\rangle = \langle y^2(t)\rangle$, we get

$$\langle x^2(t)\rangle \sim \frac{\xi}{\sqrt{\langle x^2(t)\rangle}} v^2 t^2. \tag{12}$$

For the 2D MSD $\langle \rho^2(t)\rangle = \langle x^2(t)\rangle + \langle y^2(t)\rangle$, this implies that

$$\langle \rho^2(t)\rangle \sim \xi^{2/3} v^{4/3} t^{4/3}. \tag{13}$$

Thus, here the exponent of enhanced diffusion is 4/3, smaller than that of the (1+1)D model, 3/2. The lower exponent is due to the increase in the velocity (polarity) field dimensionality d_v, changing from $d_v=1$ in the (1+1)D model to $d_v=2$ here. A similar dimensional reduction of the anomalous diffusion exponent is also found in the (2+1)D model. In the latter, the Euclidean dimension ($d=3$) is larger than in the (1+1)D model ($d=2$), but the velocity field dimensionality is the same, $d_v=1$. Indeed, departure from the usual random walk result is mostly due to the "memory" that the particle carries. Since the disorder is quenched, the particle "remembers" the polarity of a track to which it was attached in the past, and upon returning to it, it is forced to move in the same direction as before. We expect that, in higher dimensions, this correlation effect will become weaker and will lower the superdiffusion exponent towards unity. Note that in the long-time limit the MSD is independent of the processivity time τ_p (and the probability to remain on the same track, f). This will be verified in the simulations.

A more accurate self-consistent approach is based on Eq. (4), leading to the coupled equations

$$\frac{d^2}{dt^2}\langle y^2(t)\rangle = 2v^2 P_{0,x}(t), \tag{14}$$

$$\frac{d^2}{dt^2}\langle x^2(t)\rangle = 2v^2 P_{0,y}(t). \tag{15}$$

Using the symmetry between the dynamics in the x and y directions, we obtain that

$$\frac{d^2}{dt^2}\langle x^2(t)\rangle = 2v^2 P_{0,x}(t). \tag{16}$$

Assuming $P_{0,x} = C\xi(\langle x^2(t)\rangle)^{-1/2}$, where C is a numerical constant,

$$C = \frac{\gamma}{\sqrt{2}\Gamma\left(\frac{1}{2\gamma}\right)} \tag{17}$$

(for a Gaussian PDF $C = 1/\sqrt{2\pi}$), and denoting by $\phi(t) \equiv \langle x^2(t)\rangle$, Eq. (16) becomes

$$\phi^{1/2}\frac{d^2}{dt^2}\phi = 2Cv^2\xi, \tag{18}$$

with $\phi(0)=0$ and $\phi'(0)=0$. Assuming a power-law solution leads to the 2D MSD

$$\langle \rho^2(t)\rangle = 2^{1/3}(9C)^{2/3}(v^2\xi)^{2/3} t^{4/3}, \tag{19}$$

in agreement with the simple scaling approach. [For a Gaussian distribution, $2^{1/3}(9C)^{2/3} = 2.95$.]

Asymmetric network. In a more general configuration of the network, tracks along the x axis point to the right with probability p and to the left with probability $q=1-p$. Such asymmetry leads to a constant drift $\langle x(t)\rangle \simeq (p-q)vt$. Similar to dynamics in the asymmetric (1+1)D model, along the y axis we expect a crossover from the symmetric-model behavior, $\langle y^2(t)\rangle \sim t^{4/3}$, at short and intermediate times, to regular diffusion $\langle y^2(t)\rangle \sim t$ at long times. In turn, this implies that along the x axis, the MSD about the constant drift should exhibit a crossover from $\langle (x-\langle x\rangle)^2\rangle \sim t^{4/3}$ to a $\sim t^{3/2}$ behavior similar to that in the (1+1)D model. The behavior of the

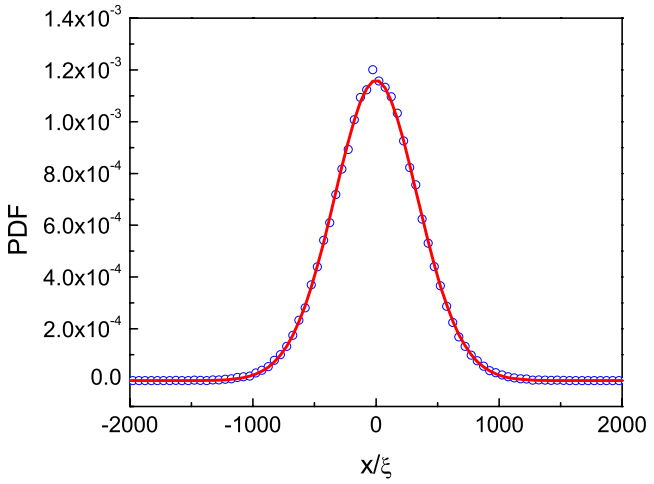

FIG. 4. (Color online) PDF along the x axis at time $t=10^5\tau_v$ for the 2D network. The circles are simulation data, and the line is the best-fitting stretched Gaussian PDF, Eq. (11), with $\gamma=0.96\pm0.01$ and $\sigma=\sqrt{\langle x^2\rangle}=340\pm1$, correlation coefficient $R=0.999$.

MSD can be further quantified using, as before, the dimensionless quantity $\delta=\frac{\sqrt{\langle\delta x^2(t)\rangle}}{|\langle x(t)\rangle|}\simeq\frac{(v^2\xi)^{1/3}t^{2/3}}{|p-q|vt}$. Here $\delta\sim1$ corresponds to the crossover and the crossover time is $t^*\simeq\frac{\xi}{v|p-q|^3}$. Therefore we expect that

$$\langle y^2\rangle\simeq\begin{cases}(9C/2)^{2/3}(v^2\xi)^{2/3}\,t^{4/3} & \text{for } t\ll t^*,\\ \dfrac{v\xi}{|p-q|}t & \text{for } t\gg t^*.\end{cases}\tag{20}$$

$$\langle(x-\langle x\rangle)^2\rangle\simeq\begin{cases}(9C/2)^{2/3}(v^2\xi)^{2/3}\,t^{4/3} & \text{for } t\ll t^*,\\ \dfrac{4\sqrt{2}}{3\sqrt{\pi}}|p-q|^{1/2}v^{3/2}\xi^{1/2}\,t^{3/2} & \text{for } t\gg t^*.\end{cases}\tag{21}$$

Note that as $|p-q|\to0$ the crossover time *diverges*, implying that *longer observation times* are required to detect the asymptotic long-time behavior, and the $\sim t^{4/3}$ behavior of the symmetric case is recovered.

Computer simulations. Computer simulations for both the symmetric and asymmetric 2D networks have been performed. We chose the probability to remain on track at intersections to be in the range $f=0.5-0.9$. This range of f gives the particle a sufficiently broad sampling of different tracks along its stochastic trajectory, while maintaining a reasonable computation time. In the symmetric 2D network, the mean position of the particle vanishes (as expected by symmetry) and, within the accuracy of the simulations, the PDF's are Gaussian. Figure 4 shows the PDF of the symmetric network along the x axis for $f=0.6$. We used 10^5 particles and 10^5 steps, where each step corresponds to the physical time $\tau_v=\xi/v$. Similar results were obtained for motion along the y axis. The numerical PDF is compared to the best-fitting stretched Gaussian, Eq. (11), with an exponent $\gamma=0.96\pm0.01$ and correlation coefficient $R=0.999$. The PDF was also compared to the best-fitting Gaussian. For this fit

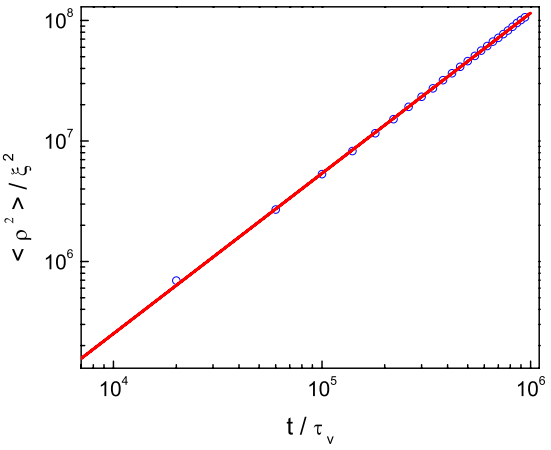

FIG. 5. (Color online) 2D MSD in the symmetric 2D network model for processivity $f=0.6$. The circles are simulation data, and the solid line is a fit to $\langle\rho^2\rangle=At^\alpha$ with $A=1.164\pm0.001$ and $\alpha=1.3331\pm10^{-4}$

$R=0.999$ and the fitted Gaussian is indistinguishable from the corresponding stretched Gaussian.

Figure 5 shows the 2D MSD fitted to a power law, $\langle\rho^2(t)\rangle=At^\alpha$ with $\alpha\simeq1.3331\pm10^{-4}$, in good agreement with the analytical value $\alpha=4/3$. The corresponding numerical prefactor is $A=1.164\pm0.001$, about one-third of the theoretical value $A=2.9542$. The origin of this discrepancy is not clear and could be due to the approximation involved in the self-consistent approach or because the simulation time does not reach the asymptotic regime. In Fig. 6 we plot the MSD for different values of the probability to stay on track f and, correspondingly, different values of the processivity time τ_p. The behavior of the MSD in the asymptotic regime is found to be independent of f, as predicted by Eq. (19), although at intermediate times we find some f dependence.

Figures 7(a) and 7(b) present simulation results for the asymmetric 2D network for processivity parameter $f=0.7$ and asymmetry $p=0.52$. Figure 7(a) shows the MSD about

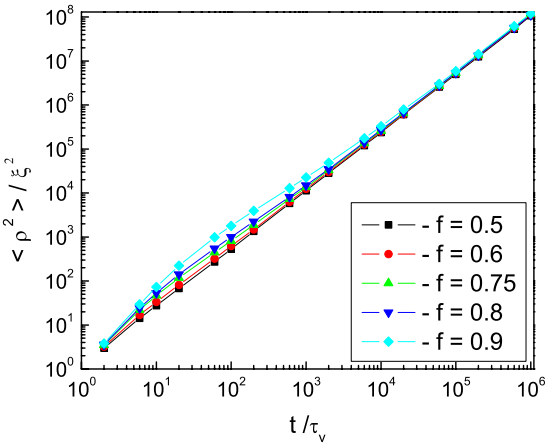

FIG. 6. (Color online) 2D MSD in the symmetric 2D network model for different processivities f in the range 0.5–0.9. Note that all curves converge to a single line in the long-time limit with $\langle\rho^2\rangle\sim t^\alpha$, $\alpha=4/3$.

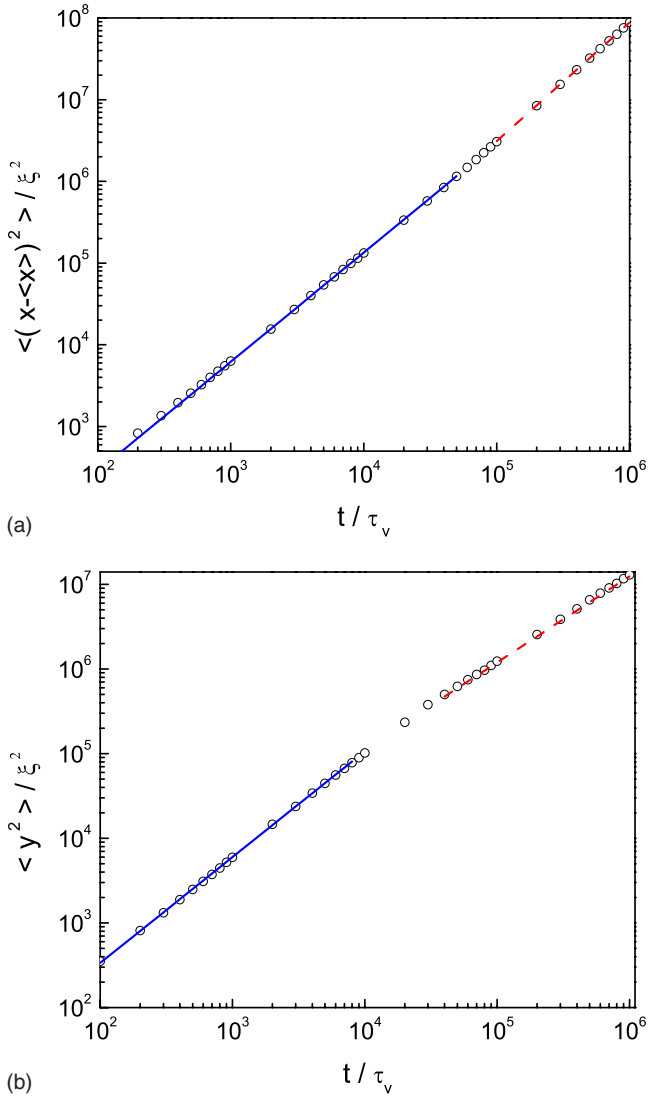

FIG. 7. (Color online) MSDs in the asymmetric 2D network for $f=0.7$ and $p=0.52$. The circles are simulation data, and the lines are fits to At^{α} in two regimes of times. (a) The MSD about the drift along the x axis, $\langle (x-\langle x\rangle)^2(t)\rangle$. For the intermediate-time regime $A=0.638\pm0.002$ and $\alpha=1.3304\pm0.0003$ (solid line); for the long time regime $A=0.1643\pm0.0002$ and $\alpha=1.4549\pm0.0001$ (dashed line). (b) The MSD along the y axis, $\langle y^2(t)\rangle$. For the intermediate time regime $A=1.101\pm0.015$ and $\alpha=1.246\pm0.002$ (solid line); for the long time regime $A=10.1\pm0.1$ and $\alpha=1.0191\pm0.0002$ (dashed line).

the drift along the x axis, for which there is a net polarity ($p\neq q$). We note the crossover from the $\sim t^{4/3}$ behavior for short and intermediate times (solid line) to the $\sim t^{3/2}$ behavior for long times (dashed line) as predicted in Eq. (21). Moreover, in Fig. 7(b) we show the MSD along the y axis, displaying a crossover from $\sim t^{4/3}$ behavior for short and intermediate times (solid line) to $\sim t$ behavior for long times (dashed line) as predicted in Eq. (20). The simulation values for the two superdiffusion exponents are close to those predicted theoretically—namely, 4/3 and 3/2 (see figure captions).

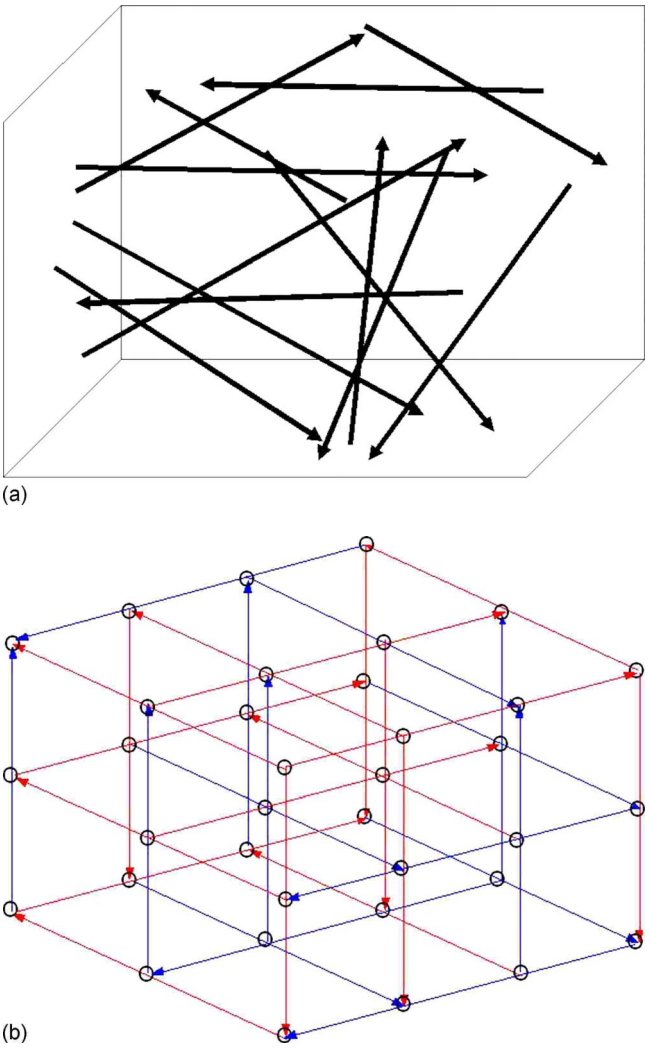

FIG. 8. (Color online) Schematic presentation of 3D microtubule networks. The arrows denote the polarity; i.e., they point towards the minus end of the microtubule. (a) 3D network with both orientational and polarity disorder. (b) 3D cubic lattice network bearing polarity disorder, but no orientational disorder.

B. Disordered 3D network

Next we consider a 3D network that is similar in topology to the 2D network, only that it has an additional dimension [see Fig. 8(b)]. As in the 2D case, it includes quenched polarity disorder. We assume that the network in Fig. 8(b) can mimic the dynamics of the more realistic network shown in Fig. 8(a). In the following, we consider both symmetric and asymmetric networks with respect to the mean polarity, and obtain results from scaling and extension to scaling via a self-consistent approach similar to the one used in 2D.

Symmetric 3D network. We commence, as before, with the scaling approach valid in the long-time regime. There, we may assume that the following relations hold:

$$\langle x^2(t)\rangle \sim P_{0,yz}(t)v^2t^2, \tag{22}$$

$$\langle y^2(t)\rangle \sim P_{0,xz}(t)v^2t^2, \tag{23}$$

$$\langle z^2(t)\rangle \sim P_{0,xy}(t)v^2t^2, \tag{24}$$

where $P_{0,\alpha\beta}$ is the probability of return to the origin of the (α,β) plane. Moreover, the scaling relations between the return probabilities and the MSDs,

$$P_{0,xy}(t) \sim \frac{\xi^2}{\sqrt{\langle x^2\rangle\langle y^2\rangle}}, \tag{25}$$

$$P_{0,yz}(t) \sim \frac{\xi^2}{\sqrt{\langle y^2\rangle\langle z^2\rangle}}, \tag{26}$$

$$P_{0,xz}(t) \sim \frac{\xi^2}{\sqrt{\langle x^2\rangle\langle z^2\rangle}}, \tag{27}$$

are also expected to hold. Using statistical equivalence between the axes, $\langle x^2(t)\rangle=\langle y^2(t)\rangle=\langle z^2(t)\rangle$, leads to the 3D MSD

$$\langle r^2(t)\rangle \sim v\xi t. \tag{28}$$

Note that the time dependence is diffusivelike, $\langle r^2\rangle \sim t$, despite the active nature of the transport. We attribute this behavior to the effect of increased dimensionality, as explained after Eq. (13).

Next, we use a more accurate approach that relies on Eq. (4) and the statistical equivalence of the axes to obtain a differential equation for the 1D MSD $\phi(t)\equiv\langle x^2(t)\rangle$,

$$\phi\frac{d^2}{dt^2}\phi = 2C^2v^2\xi^2, \tag{29}$$

with the initial conditions $\phi(0)=0$ and $d\phi/dt|_0=0$. (The same equation also holds for the MSD along y and z.) Solving analytically Eq. (29) is possible; see Appendix B. However, the solution is implicit and we therefore concentrate on the limit $t \gg \tau_v$, where $\tau_v=\xi/v$. The asymptotic solution for this limit is derived in Appendix A using directly Eq. (29) and, in Appendix B, using the formal exact solution. Consequently, the 3D MSD is

$$\langle r^2\rangle \simeq 6Cv\xi t\left(\ln\frac{t}{\tau_v}\right)^{1/2}. \tag{30}$$

This represents a weak correction to the scaling diffusivelike result $\langle r^2\rangle \sim t$ in terms of a sublogarithmic factor $(\ln t)^{1/2}$.

Asymmetric 3D network. In the asymmetric version of the 3D network, tracks along the x axis point to the right with probability p and to the left with probability $q=1-p$. The dynamics along the other two axes y and z remains symmetric. We therefore expect a constant drift $\langle x(t)\rangle \simeq (p-q)vt$ along the x axis. Consider now the motion along the y axis. While at intermediate times we expect $\sim t(\ln t)^{1/2}$ behavior as in the symmetric case, at long times the MSD will grow linearly with time. The latter is due to the polarity randomization along y that, in turn, results from the constant drift along the x axis. The same behavior is expected in the z direction; however, such crossover is barely observable. Similar behavior is expected for the MSD (about the drift) along the x axis. At intermediate times the MSD grows as $\sim t(\ln t)^{1/2}$. Since in the (y,z) plane motion is asymptotically diffusive, we expect the long-time MSD (about the drift) along the x axis to behave in the same way as the MSD of the (2+1)D RVM discussed in Sec. II—i.e., $\sim t\ln t$. Once again, such crossover is barely noticeable, and therefore we will not pursue the study of this model.

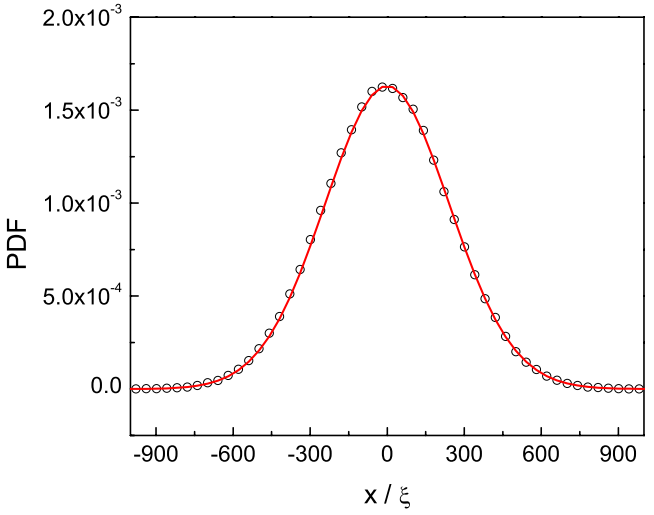

FIG. 9. (Color online) PDF along the x axis for processivity $f=0.6$ and at time $t=10^5\tau_v$ for the 3D network. The circles are simulation data, and the line is the best-fitting stretched Gaussian PDF, Eq. (11), with $\gamma=0.983\pm0.006$ and $\sigma=\sqrt{\langle x^2\rangle}=244.6\pm0.6$, correlation coefficient $R=0.9999$.

Computer simulations. Computer simulations of the *symmetric* 3D network have been carried out. As for the 2D network, we assign at each junction a probability $f=0.6$ for the particle to remain on the track on which it is moving and a probability $1-f$ to bind to one of the two perpendicular tracks (with equal probabilities). We have verified that the mean position of the particle vanishes as required by symmetry. Figure 9 shows the PDF along the x axis for $f=0.6$. We used 3×10^4 particles and 10^5 steps; each step corresponds to a time $\tau_v=\xi/v$. The PDF is compared to the best-fitting stretched Gaussian, Eq. (11), with $\gamma=0.983\pm0.006$ ($R=0.9999$). The PDF was also compared to the best-fitting Gaussian. For this fit $R=0.9997$ and the fitted Gaussian is indistinguishable from the corresponding stretched Gaussian. Both fits show that, within the accuracy of our simulations, the PDF is essentially Gaussian.

Figures 10(a) and 10(b) display the behavior of the 3D MSD at long times. In Fig. 10(a), the horizontal axis is $t(\ln t)^{1/2}$ (log scale) and the MSD is compared to the best-fitting $At(\ln t)^{1/2}$, yielding $A=3.3126\pm0.0004$. On the other hand, in Fig. 10(b) the horizontal axis is $\ln t$ (log scale) and the MSD, which is divided by t in this plot, is compared to the best fitting $At(\ln t)^{\beta}$, yielding $\beta=0.1132\pm0.0001$ and $A=3.365\pm0.001$. While this value of β does not agree with the analytical result $\beta=1/2$, the prefactor A is not too far from the corresponding prediction $A=2.394$.

C. Plane-oriented 3D network

Recently, transport in *in vitro* microtubule networks, with topology similar to that depicted in Fig. 11(a), has been studied [13]. While in this system microtubules are nearly ori-

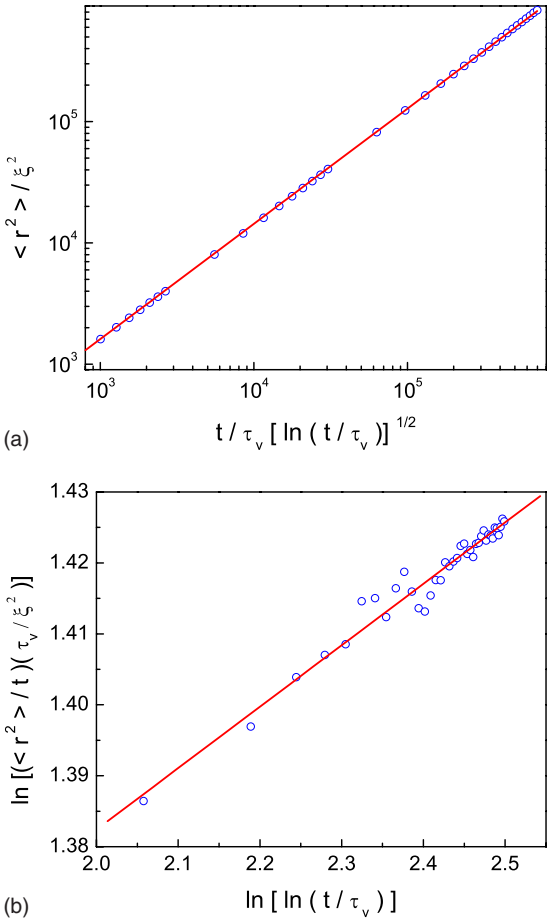

FIG. 10. (Color online) MSD in the 3D network model for processivity $f=0.6$. The circles are simulation data, and the solid lines are fitting functions. (a) Plot of $\langle r^2 \rangle$ vs $t(\ln t)^{1/2}$; fitting function $\langle r^2 \rangle = At[\ln \frac{t}{\tau_v}]^{1/2}$ with $A=3.3126 \pm 0.0004$. (b) Plot of $\frac{\langle r^2 \rangle}{t}$ vs $\ln t$; fitting function $\langle r^2 \rangle = At(\ln t)^{\beta}$ with $\beta=0.1132 \pm 0.0001$ and $A=3.365 \pm 0.001$.

ented in the 2D plane, the orientation distribution of filaments within this plane is isotropic. Cargo particles that posses a nuclear localization signal were shown to be carried mostly or entirely by dynein motor proteins. Surprisingly, the MSD obtained from single-particle tracking data shows nearly diffusive behavior. This is somewhat counterintuitive, since one would naively expect active transport to lead to superdiffusive dynamics. However, in view of our results in the previous section, these measurements may be understood within the framework of disordered networks.

Our model for the experimental system in Ref. [13] is shown in Fig. 11(b). It consists of planes on which the orientation of microtubules alternates. Overall, the system is isotropic in the projected 2D plane. Since the topology of the network in Fig. 11(b) has the same key features as the experimental system depicted in Fig. 11(a), we believe that both networks belong to the same "universality class;" namely, their corresponding anomalous diffusion exponents are equal. The polarity of the microtubules is random with 50% probability for each direction. The motion of the cargo particle includes stepping along the microtubules with a finite probability to disconnect and random walks between the

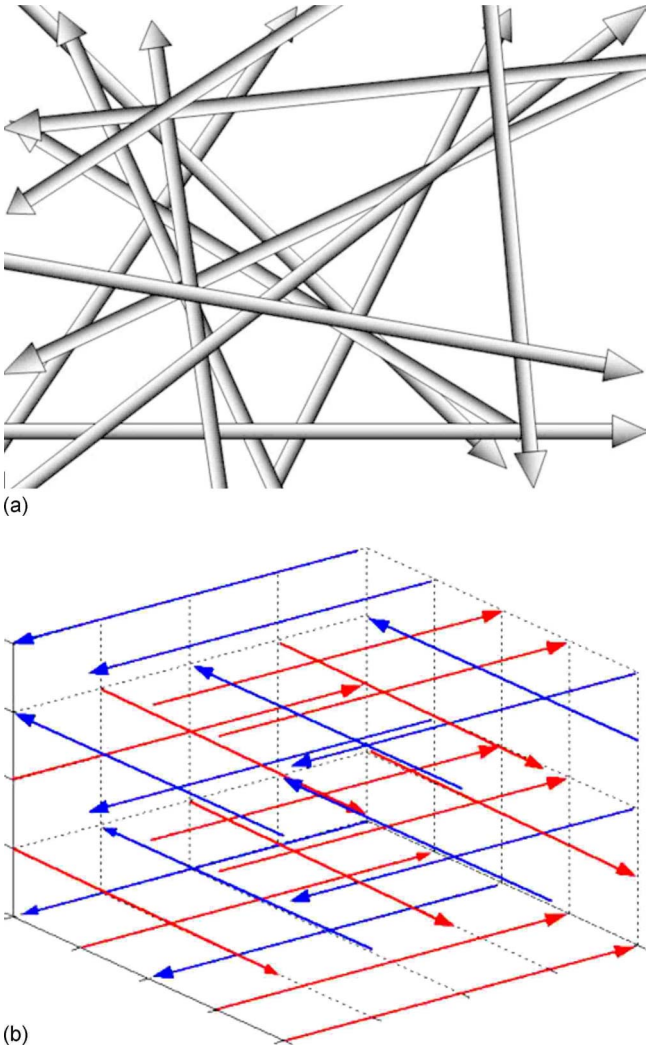

FIG. 11. (Color online) Schematic presentation of the plane-oriented 3D network. The arrows denote the polarity; i.e., they point towards the minus end of the microtubule. (a) Network where the microtubules are partially oriented in 2D, but where both orientational and polarity order within the 2D plane are absent. (b) Network consisting of alternating (1+1)D model planes, bearing polarity disorder within each plane, but no orientational disorder.

filaments. Thus, the structure within each plane is identical to that of the (1+1)D model. A summary of the main results for this model has been presented in Ref. [13] in conjunction with the experimental results. Below we elaborate on the analytical derivation and include simulation results. In addition, we expand our study to include the diffusion of the cargo in the bulk solution. Although this does not change the scaling of the MSD with time, it allows a more detailed comparison with experiment. We focus here only on the symmetric network case since, just as for the 3D network, the effect of asymmetry is marginal.

We commence with the scaling approach. The only modification with respect to the 3D network model is that along the z axis there is only diffusive transport that is independent of the motion on microtubules, $\langle z^2(t) \rangle \simeq 2D_z t$. Therefore, in the long-time limit we expect that

$$\langle x^2(t) \rangle \sim P_{0,yz}(t) v^2 t^2, \tag{31}$$

$$\langle y^2(t)\rangle \sim P_{0,xz}(t)v^2t^2, \tag{32}$$

where

$$P_{0,yz}(t) \sim \frac{\xi^2}{\sqrt{D_z t\langle y^2\rangle}}, \tag{33}$$

$$P_{0,xz}(t) \sim \frac{\xi^2}{\sqrt{D_z t\langle x^2\rangle}}. \tag{34}$$

Using the statistical equivalence between the x and y axes, $\langle x^2(t)\rangle = \langle y^2(t)\rangle$, leads to the 2D MSD $\langle \rho^2(t)\rangle = \langle x^2\rangle + \langle y^2\rangle$:

$$\langle \rho^2(t)\rangle \sim \frac{(v\xi)^{4/3}}{D_z^{1/3}}t. \tag{35}$$

As before, the time dependence is diffusivelike, $\langle \rho^2\rangle \sim t$, despite the active transport.

Next we use the more accurate self-consistent approach. Applying Eq. (4) to the present geometry reads

$$\frac{d^2}{dt^2}\langle y^2(t)\rangle = 2v^2P_{0,xz}(t), \tag{36}$$

$$\frac{d^2}{dt^2}\langle x^2(t)\rangle = 2v^2P_{0,yz}(t), \tag{37}$$

where

$$P_{0,yz}(t) = \frac{C\xi^2}{\sqrt{4\pi D_z t\langle y^2\rangle}}, \tag{38}$$

$$P_{0,xz}(t) \sim \frac{C\xi^2}{\sqrt{4\pi D_z t\langle x^2\rangle}}, \tag{39}$$

and C is given by Eq. (17). Using the statistical equivalence between the two axes x and y, we obtain, for $\phi(t) = \langle x^2\rangle = \langle y^2\rangle$,

$$\phi^{1/2}\frac{d^2}{dt^2}\phi = \frac{B}{t^{1/2}}, \tag{40}$$

where

$$B = \frac{C}{\sqrt{\pi}}\frac{v^2\xi^2}{D_z^{1/2}}. \tag{41}$$

While we were not able to obtain the analytical solution of Eq. (40), the asymptote of the 2D MSD at long times is (see Appendix A)

$$\langle \rho^2(t)\rangle \simeq 2^{1/3}(3B)^{2/3}t\left[\ln\left(\frac{t}{\tau_v}\right)\right]^{2/3}, \tag{42}$$

where $\tau_v = \xi/v$. As for the random 3D network, here too we find a small, sublogarithmic, correction to the scaling result $\langle \rho^2\rangle \sim t$, implying that the motion is barely distinguishable from regular diffusion.

Computer simulations. The simulated network is shown in Fig. 11(b). At each *virtual* junction—i.e., a junction that appears on the projection of two neighboring (x,y) planes—the particle has probability f to remain on a track and $1-f$ to leave the track. If it leaves the track, it hops to one of the four neighboring tracks with equal probabilities: the two tracks that are parallel to the source track (same plane of orientation) and the two tracks that are perpendicular to the source track (neighboring planes of orientation). The simulations were performed for the particular choice $D_z = \frac{v\xi}{2}$ and $f = 0.5$.

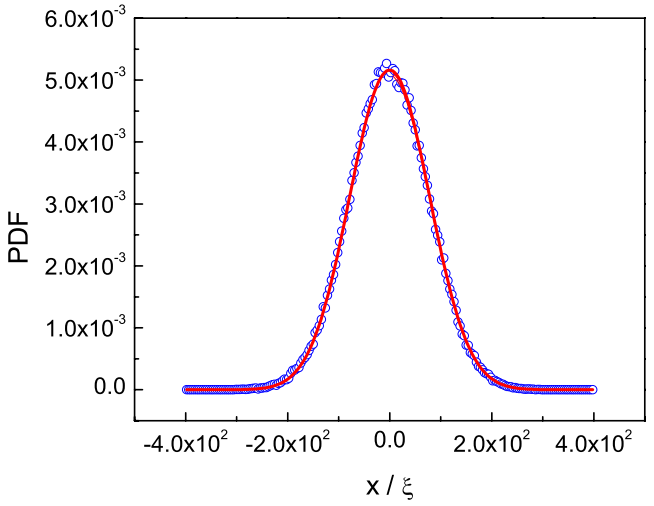

FIG. 12. (Color online) PDF along the x axis for processivity $f = 0.5$ and at time $t = 10^4\tau_v$ for the plane-oriented 3D network. The circles are simulation data, and the line is the best-fitting stretched Gaussian PDF, Eq. (11), with $\gamma = 1.014 \pm 0.008$ and $\sigma = \sqrt{\langle x^2\rangle} = 77.7 \pm 0.2$, correlation coefficient $R = 0.9997$.

Figure 12 shows the PDF along the x axis for 10^4 computer steps and 2×10^5 particles. The stretched Gaussian provides a good fit to the data, yielding a stretching exponent very close to 1 ($\gamma = 1.014 \pm 0.008$), and the use of a Gaussian makes no essential difference (not shown). Figures 13(a) and 13(b) show the (x,y) plane 2D MSD at long times. In Fig. 13(a) the horizontal axis is $t(\ln t)^{2/3}$ and the MSD is compared to the best fitting $At(\ln t)^{2/3}$, yielding $A = 1.05 \pm 0.04$. This result is in good agreement with the analytical prediction $A = 1.22$. Moreover, in Fig. 13(b) the horizontal axis is $\ln t$ and the MSD, divided by t, is compared to the best-fitting $At(\ln t)^{\beta}$, yielding $A = 1.05 \pm 0.04$ and $\beta = 0.63 \pm 0.02$, in agreement with the prediction $\beta = 2/3$.

To provide a more realistic model of the transport, we included the diffusion in a bulk solution and the attachment-detachment processes between the solution and the microtubules. For this, we use a finer grid on which the random walk that models the diffusion in the solution takes place. Since the ratio of the physical mesh size ξ to grid size a that we use is 10, there are nine sites between neighboring filaments that represent the solution. When the particle hops from a bulk site to a microtubule site, it has a probability $\bar{f}$ to attach, in which case it proceeds to move along the microtubule. A particle that moves along a microtubule has, at each grid point, a probability $\bar{f}$ to remain on the track and $1-\bar{f}$ to fall off—that is, to hop to one of its four neighboring grid sites of the solution. Note that the processivity parameter $\bar{f}$ here is different from the one defined before, f. The latter determines the probability to remain on the track at a network

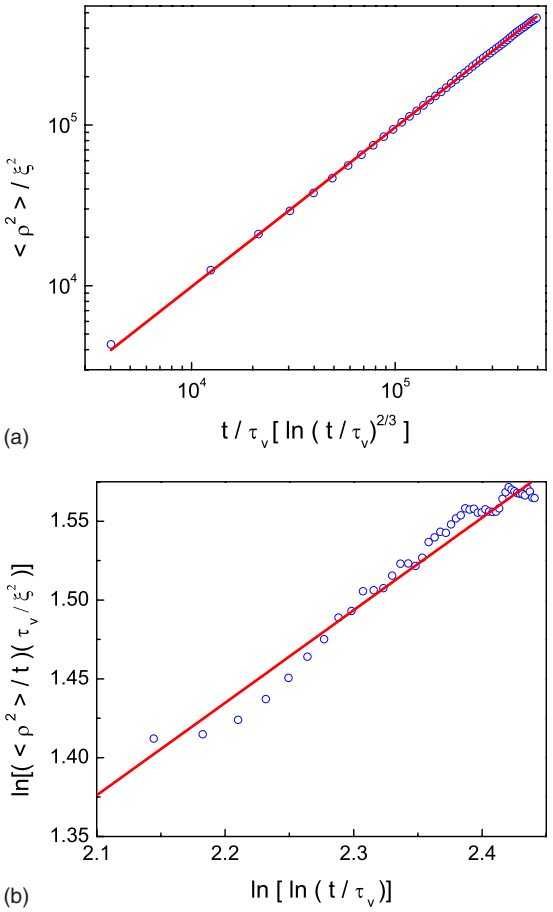

FIG. 13. (Color online) MSD in the plane-oriented 2D network model for processivity $f=0.5$. The circles are simulation data, and the solid lines are fitting functions. (a) Plot of $\langle r^2 \rangle$ vs $t(\ln t)^{2/3}$; fitting function $\langle r^2 \rangle = At[\ln \frac{t}{\tau_0}]^{2/3}$ with $A=1.05 \pm 0.04$. (b) Plot of $\frac{\langle r^2 \rangle}{t}$ vs $\ln t$; fitting function $\langle r^2 \rangle = At(\ln t)^{\beta}$ with $\beta=0.63 \pm 0.02$ and $A=1.05 \pm 0.04$.

mesh point, implying that f and $\bar{f}$ are related by $f=\bar{f}^m$, $m=\xi/a$.

Figure 14 shows the MSD behavior for 10^4 particles, taking $\bar{f}=0.975$, $\xi/a=10$, and $v=0.01(a/\tau_0)$, where τ_0 is the hopping time on the grid. Note that the MSD is normalized by a^2 rather than by ξ^2 and that time is measured in units of τ_0. We find that the normalized MSD increases as $A(t/\tau_0)[\ln(t/\tau_0)]^{\beta}$ with $\beta=0.641 \pm 0.002$ and $A=0.0988 \pm 0.0004$. The value of β is close to the theoretical value $2/3$ and is in agreement with the diffusion-free simulations discussed above. Using the random walk expression $D_z=\frac{a^2}{2\tau_0}$ in Eq. (42), we find that the theoretical prefactor is $A=0.0567$, similar to the numerical value. As expected, including the details of bulk diffusion and attachment-detachment processes did not change the scaling behavior in time. It merely determined the timescale for the diffusive motion between filaments.

D. Three-dimensional animal cell model

While the models studied above are important for the analysis of previous and future *in vitro* experiments, they do not provide full insight into the transport mechanisms in the living cell. In particular, we seek to establish the purpose of the finite processivity, as modeled by the processivity parameter f, for transport in the cell. For this reason, we designed a 3D model in which the (animal) cell is modeled as a cube; see Fig. 15. In this model, all microtubules originate from the origin $\vec{r}=0$, the center of the box, representing the centrosome. To mimic the network disorder that was observed in animal cells (see Ref. [1], p. 807), the microtubule configuration is modeled as a biased random walk on a 3D simple cubic lattice, starting from the origin towards the membrane. To allow for a high microtubule density near the origin, we do not include an excluded-volume interaction between filaments. While the microtubules' minus ends are connected to the centrosome (the origin) and their plus ends terminate at the membrane, in between there remains significant configurational disorder. As the cargo particles walk on the microtubules, at each grid point they have a finite probability f to stay on the filament and continue walking on it and a probability $1-f$ to fall off the filament and hop to one of the available nearest grid points, whether it is occupied by another microtubule or simply a solution site. If the particle falls off the microtubule, it performs regular random walk on the grid until it reaches another filament, attaching to it with probability f. The linear dimension of the cubic cell is 100ξ, where ξ here is the lattice constant, such that the membrane is located on the planes $x=\pm 50\xi$, $y=\pm 50\xi$, and $z=\pm 50\xi$.

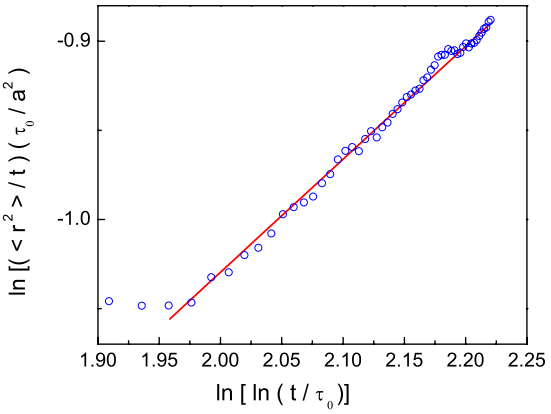

FIG. 14. (Color online) MSD in the plane-oriented 2D network where thermal diffusion in the solution is included for $\bar{f}=0.975$, $\xi/a=10$, and $v=0.01(a/\tau_0)$. Note that the MSD is normalized by a^2 and that time is measured in units of τ_0. The circles are simulation data, and the solid line is a fit to $A(t/\tau_0)[\ln(t/\tau_0)]^{\beta}$ with $\beta=0.641 \pm 0.002$ and $A=0.0988 \pm 0.0004$.

Since here the MSD is not an appropriate measure of the efficiency of transport, we study various "first-passage-time" (or "first-arrival" and "first-exit") problems in which the cargo has to reach a certain target in the cell. We consider the probability of the cargo to reach the target until time t, $P_{\text{exit}}(t)$, the derivative of which represents the probability per unit time (i.e., the flux) of the particle to arrive, for the first time, at the target at time t. We examine three cases differing from each other in the starting location and/or the target location: (i) cargo originating at the centrosome (which is usually near the nucleus) and having to reach the membrane via

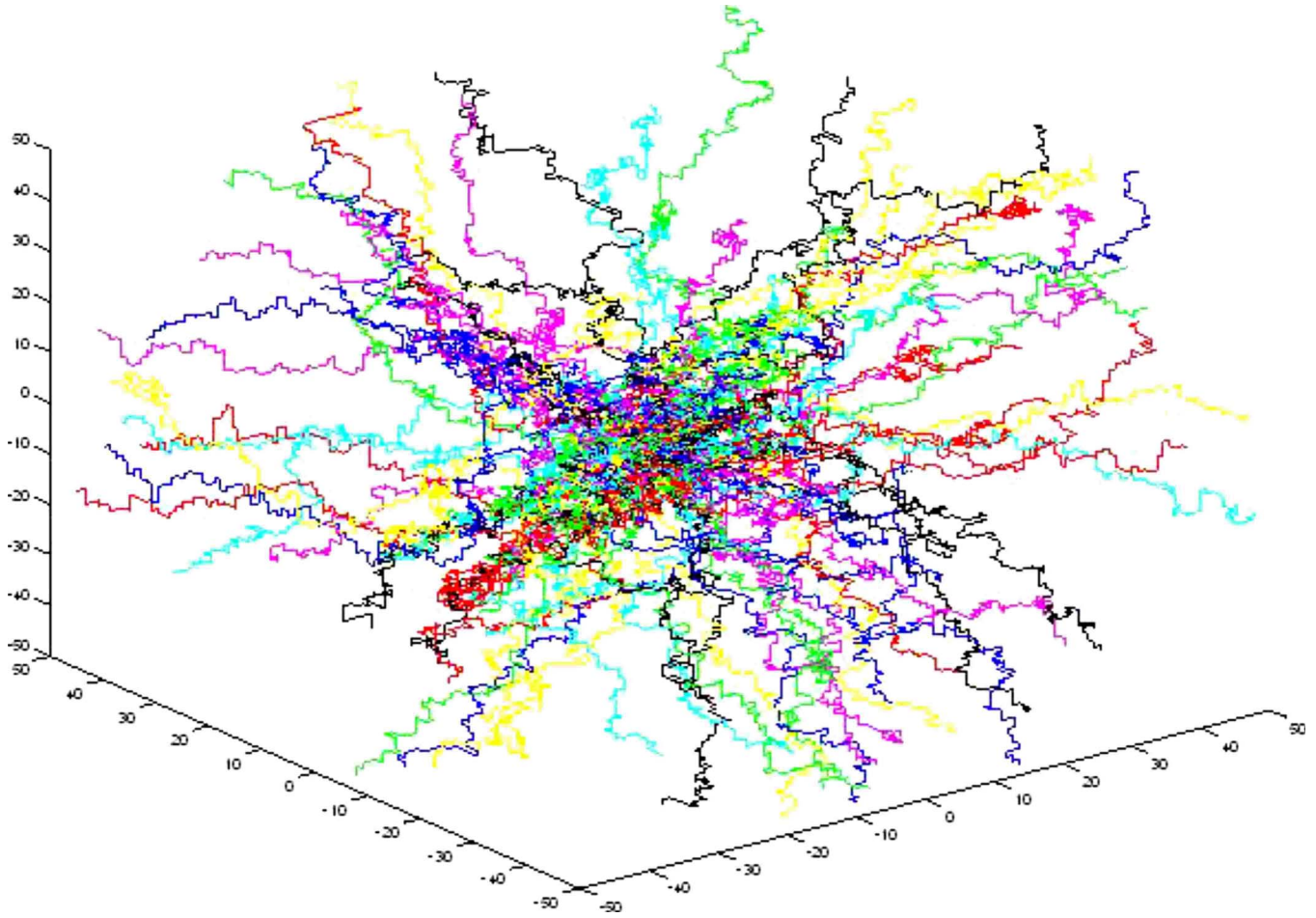

FIG. 15. (Color online) The 3D cell model used for the simulations in one of its realizations. The box size is $100\times100\times100$. The centrosome is at the origin $\vec{r}=(0,0,0)$, and the membrane is situated at the box surface. Microtubules were simulated as a biased, phantom (non-self-avoiding), random walk that starts at the origin and ends at the box surface. The results shown in Figs. 16–18 were obtained by averaging over 100 realizations of the network.

kinesin-mediated transport, (ii) cargo originating at the membrane and having to reach a small region around the centrosome—i.e., a unit box—via dynein-mediated transport, (iii) cargo leaving the centrosome and having to reach, via kinesin-mediated transport, a localized target in the cytoplasm. The target is represented by a cube of linear dimension 10ξ centered at $\vec{r}=(25,25,25)$. In case (iii) we examine two different boundary conditions at the membrane: reflective boundary condition and "radiative boundary conditions." In the latter case, when the particle reaches the membrane, it may be "absorbed" (or expelled from the cell) with a finite probability w, mimicking an exocytosis process. In particular, $w=0$ corresponds to absence of exocytosis ("reflective boundary conditions"), whereas $w=1$ represents perfect exocytosis efficiency ("absorbing boundary conditions"), albeit unrealistic. In all three cases we consider different processivities.

All our results for this model, shown in Figs. (16)–(18), were obtained from computer simulations. In cases (i) and (ii), 100 realizations of the network were randomly chosen and 100 particles were simulated for each network. In case (iii), simulations were performed for 50 random realizations of the network and 300 different particles for each network. The results were averaged over all runs, from all the networks, to obtain the behavior in the "average" cell. For simplicity, the bulk diffusion time scale τ_0 and the active motion timescale $\tau_v=\xi/v$ were set to be equal. In each case we compute the first arrival probability $P_{\text{exit}}(t)$.

In Fig. 16, we show the probability to reach the membrane until time t for kinesin-mediated transport of a particle that starts at the centrosome at $t=0$ and for different values of f [case (i)]. We find that as processivity increases, so does the efficiency of transport. In this case, diffusion is less efficient than active motion along filaments. This is intuitively clear, as all microtubule plus ends terminate at the membrane, implying that the best choice for the cargo particle is to stay on its track. The same is true for the probability to reach the centrosome (or nucleus) starting at the membrane in dynein mediated transport [case (ii)]; see Fig. 17. Here P_{exit} is much more sensitive to motor processivity than in case (i), which is due to the inefficiency of the diffusion process to reach the origin.

However, when we consider the probability to reach a localized target in the cell starting from the centrosome (via kinesin-mediated transport), the higher the processivity, the lower is the first arrival probability at long times; see Figs.

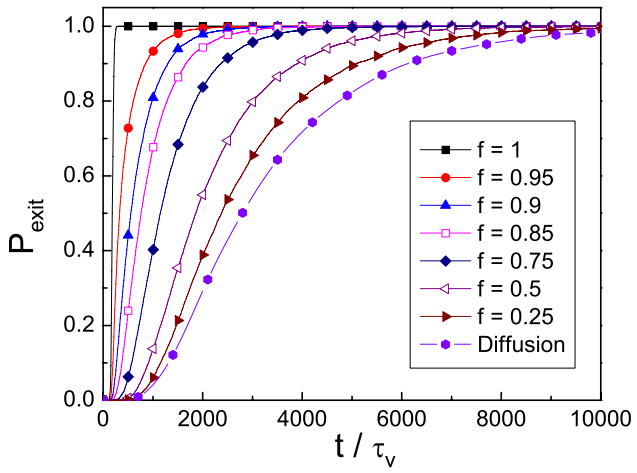

FIG. 16. (Color online) First-passage-time problem, nucleus to membrane. The probability of cargo originating at the centrosome to reach, for the first time, the membrane until time t, via kinesin-mediated transport. Different motor processivities f are shown. Free diffusion, with hopping time τ_0 equal to τ_v (the time it takes for a motor to move a mesh size ξ), is also shown for comparison.

18(a)–18(c). Moreover, here diffusion is more efficient, at long times, than active motion along filaments. This is due to the fact that most initial, randomly chosen, tracks do not lead to the target and therefore the cargo has to change tracks along the way or simply diffuse in the bulk (i.e., the cytoplasm) to reach the target. Note, however, that in the short-time regime of both boundary conditions [Figs. 18(a) and 18(c)], higher processivity increases the first arrival probability. This is due to the very few tracks that do pass through the target and on which the particle occasionally starts its motion. Processivity values are much more influential in the radiative boundary conditions case, Fig. 18(a), than in reflective boundary conditions case, Figs. 18(b) and 18(c). This occurs since higher processivity increases the chance of a particle to reach the membrane, and thus be removed from the cytoplasm (with probability w) when radiative boundary conditions are present. The reason for the simple diffusion to be the more efficient process, in the long-time limit, is also a consequence of our choice of time scales $\tau_0=\tau_v$. This may change somewhat if local motion along tracks is faster than diffusion ($\tau_v<\tau_0$), a possible situation in the dense cytoplasm.

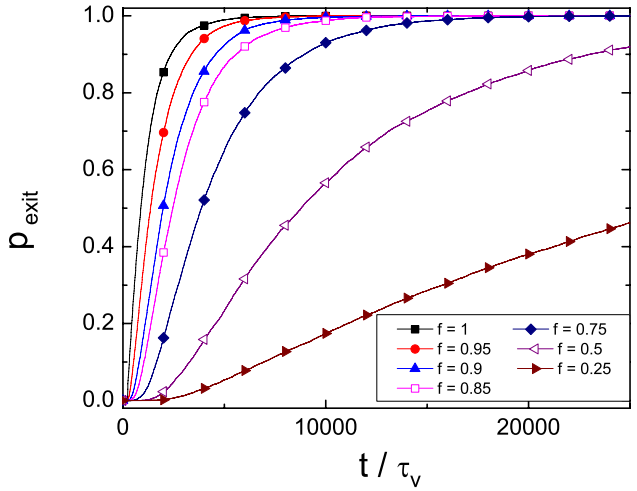

FIG. 17. (Color online) First-passage-time problem, membrane to nucleus. The probability of cargo originating at the membrane to reach, for the first time, the centrosome until time t, via dynein-mediated transport. Different motor processivities f are shown.

IV. CONCLUSIONS

Active transport on disordered microtubule networks, involving only one type of motor proteins (be it kinesin or dynein), is analogous to transport on random velocity networks. This is true because microtubules are relatively stiff "semiflexible" polymers that form roughly straight rods. Therefore, when they do not grow from a centrosome, microtubule networks display orientational and polarity disorder. In addition, this analogy holds only as long as small cargo particles, which can pass freely through the mesh, are considered. Otherwise, when the particle is larger than the mesh of the network, it will have to deform the network and move against its viscoelastic resistance [16,17]. If the cargo can alternate between kinesin and dynein during transport or attaches to both of them at the same time [16,17], this analogy is no longer valid, or in the least has to be modified.

All the model networks studied lead to superdiffusion—i.e., an MSD exponent larger than 1. As the Euclidean dimensionality and/or the velocity field ("polarity field") dimensionality of the network increases, the superdiffusion exponent decreases and approaches unity. For example, the simple (1+1)D model leads to $\sim t^{3/2}$, the 2D network leads to $\sim t^{4/3}$, the plane-oriented 3D network leads to $\sim t(\ln t)^{2/3}$, and the 3D network leads to $\sim t(\ln t)^{1/2}$. In the latter two 3D networks, motion is nearly diffusive and only slightly, sublogarithmically, enhanced. The plane-oriented 3D network has been recently studied experimentally showing such diffusivelike behavior, even though the transport was confirmed to be of active, dynein mediated, type [13].

The reason for the reduction of the superdiffusion exponent can be understood in terms of the particle "loss of effective memory" as the dimensionality grows. Regular random walk are completely Markovian as at each step the move is completely uncorrelated with the previous step. A particle moving on a *quenched* random velocity network can be viewed as possessing memory: it "remembers" the polarity of the track it moved on and will always move in the same direction whenever it returns to it. But as dimensionality grows, the return probability to a particular track decreases, reducing this correlation effect. Evidently, in the 3D networks this memory has essentially no effect.

Transport on networks originating from a centrosome can mimic active transport in the living cell. It is difficult to provide an accurate description of intracellular transport, since in the cell the disorder of the microtubule network is ill characterized and there are many unknown parameters. Nevertheless, the 3D cell model used here is sufficiently complex to reproduce the role of the finite motor processivity. The processivity in our lattice model is represented by the probability f to stay on the microtubule at a grid point, with f

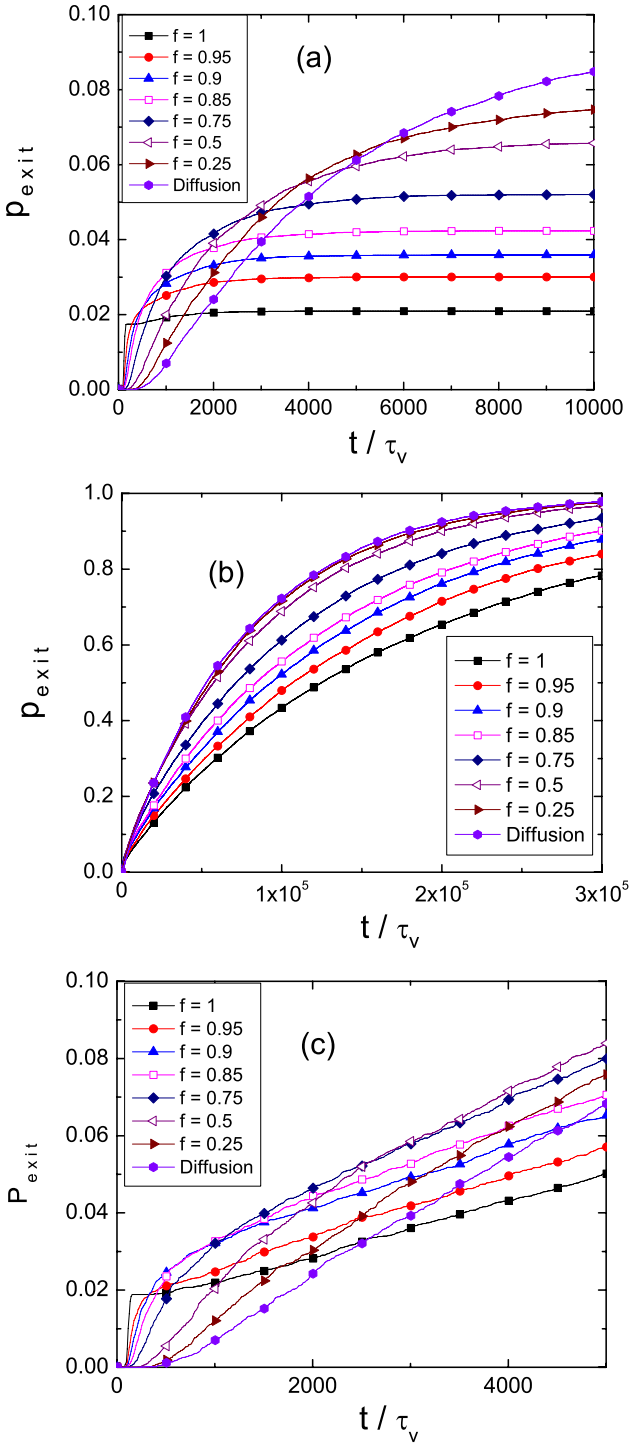

FIG. 18. (Color online) First-passage-time problem, nucleus to a localized target in the cytoplasm. The probability of cargo originating at the nucleus to reach, for the first time, a localized target in the cytoplasm until time t, via kinesin-mediated transport. The target is centered around $\vec{r}=(25,25,25)$ and is taken as a box of linear size 10. Different motor processivities f are shown. Free diffusion, with hopping time τ_0 equal to τ_v (the time it takes a motor to move a mesh size ξ), is shown for comparison. (a) Radiative boundary conditions at the membrane surface, where the probability of exit at the surface is $w=0.01$. (b) Reflective boundary conditions at the membrane surface, $w=0$. (c) The short-time behavior for reflective boundary conditions at the membrane surface (b).

=1 corresponding to infinite processivity time ("infinite processivity"). We have found that while infinite processivity is best for transport from the nucleus to the membrane or for the reverse, reaching a localized target in the cell is best achieved at small motor processivities. We suggest that motor proteins have an intermediate, finite, processivity, *in order to optimize the efficiency of transport* among the various tasks of the network.

ACKNOWLEDGMENTS

We are grateful to H. Salman and J. Klafter for illuminating discussions and to the anonymous referee suggesting the exact solution to Eq. (29). This research was supported in part by The Israel Science Foundation (RG ,Grant No. 460/06). M.E. acknowledges support from the Minerva Research Foundation.

APPENDIX A: ASYMPTOTIC SOLUTIONS OF EQS. (29) AND (40)

Equations (29) and (40) can be written in the unified form

$$\phi^{\mu}\frac{d^2}{dt^2}\phi = Bt^{-\nu}. \tag{A1}$$

For Eq. (29), $\mu=1$, $\nu=0$, and $B=2C^2v^2\xi^2$. For Eq. (40), $\mu=1/2$, $\nu=1/2$, and B is given by Eq. (41). We attempt a solution of the form $\phi=At[\ln(\frac{t}{\tau_v})]^{\beta}$. The left-hand side of Eq. (A1) becomes

$$A^{1+\mu}\beta t^{\mu-1}\left[\ln\left(\frac{t}{\tau_v}\right)\right]^{\beta+\mu\beta-1} + A^{1+\mu}\beta(\beta-1)t^{\mu-1}\left[\ln\left(\frac{t}{\tau_v}\right)\right]^{\beta+\mu\beta-2}. \tag{A2}$$

Equation (A2) cannot be made exactly equal to $Bt^{-\nu}$, since the power of the $\ln(\cdots)$ is not the same in the two terms. However, the second term is smaller than the first one by a factor of $\sim\ln(\frac{t}{\tau_v})$. Therefore, for very long times compared to τ_v, this term can be neglected. Demanding that only the first term in Eq. (A2) be equal to $Bt^{-\nu}$ leads to the following requirements: (i) $1-\mu=\nu$, (ii) $\beta+\mu\beta-1=0$, and (iii) $A^{1+\mu}\beta=B$. The condition $1-\mu=\nu$ is satisfied for both cases ($\mu=1$, $\nu=0$ and $\mu=1/2$, $\nu=1/2$), and from the two other conditions we find the unknown parameters β and A: $\beta=1/(1+\mu)$ and $A=[B(1+\mu)]^{1/(1+\mu)}$. We conclude that the asymptotic solution $\phi=At[\ln(\frac{t}{\tau_v})]^{\beta}$ is reached only when t is several orders of magnitude larger than τ_v, although it is approximately valid at shorter times; e.g., for $t/\tau_v\sim10^4$ the error is roughly 10%.

APPENDIX B: EXACT FORMAL SOLUTION OF EQ. (29)

Equation (29) can be solved exactly. Writing in the form of Eq. (A1),

$$\phi\frac{d^2}{dt^2}\phi = B, \tag{B1}$$

we multiply both sides by $\phi^{-1}\frac{d\phi}{dt}$ to get

$$\frac{d}{dt}\left[\frac{1}{2}\left(\frac{d\phi}{dt}\right)^2\right] = B\frac{d}{dt}\ln\phi. \tag{B2}$$

Integrating once we get

$$\frac{d\phi}{dt} = \sqrt{2B}\left[\ln\left(\frac{\phi}{\phi_0}\right)\right]^{1/2}, \tag{B3}$$

where ϕ_0 is a constant of integration. Integrating once more leads to the formal solution

$$\sqrt{\pi}\phi_0 i^{-1}\,\mathrm{erf}\left[i\left(\ln\left(\frac{\phi}{\phi_0}\right)\right)^{1/2}\right] = \sqrt{2B}(t-t_0), \tag{B4}$$

where $\mathrm{erf}(x)$ is the error function, $i=\sqrt{-1}$, and t_0 is a constant of integration such that $\phi(t_0)=\phi_0$, $\frac{d\phi}{dt}|_{t_0}=0$.

Equation (B4) allows a systematic asymptotic expansion in time for $t \gg t_0$ and $\phi \gg \phi_0$. Here we recover only the leading term, also derived in Appendix A. For large x, $i^{-1}\mathrm{erf}(ix) \simeq \frac{e^{x^2}}{\sqrt{\pi}x}$, such that for large t

$$\frac{\phi}{[\ln(\phi/\phi_0)]^{1/2}} \simeq \sqrt{2Bt}. \tag{B5}$$

A single iteration yields the leading behavior

$$\phi \simeq \sqrt{2Bt}\left[\ln\left(\frac{\sqrt{2B}}{\phi_0}t\right)\right]^{1/2}. \tag{B6}$$

[1] B. Alberts, D. Bray, J. Lewis, M. Raff, K. Roberts, and J. D. Watson, *Molecular Biology of the Cell*, 3rd edition (Garland, New York, 1994).
[2] J. Howard, *Mechanics of Motor Proteins and the Cytoskeleton* (Sinauer Associates, Sunderland, 2001).
[3] N. Hirokawa, Science **279**, 519 (1998).
[4] R. Mallik and S. P. Gross, Physica A **372**, 65 (2006).
[5] D. McDonald, M. A. Vodicka, G. Lucero, T. M. Svitkina, G. G. Borisy, M. Emerman, and T. J. Hope, J. Cell Biol. **159**, 441 (2002).
[6] M. Suomalainen, M. Y. Nakano, S. Keller, K. Boucke, R. P. Stidwill, and U. F. Greber, J. Cell Biol. **144**, 657 (1999).
[7] B. Sodeik, J. Cell Biol. **159**, 393 (2002).
[8] H. Mabit, M. Y. Nakano, U. Prank, B. Saam, K. Döhner, B. Sodeik, and U. F. Greber, J. Virol. **76**, 9962 (2002).
[9] G. Seisenberger, M. U. Ried, T. Endreß, H. Büning, M. Hallek, and C. Bräuchle, Science **294**, 1929 (2001).
[10] F. Nédélec, T. Surrey, and A. C. Maggs, Phys. Rev. Lett. **86**, 3192 (2001).
[11] L. Romberg, D. W. Pierce, and R. D. Vale, J. Cell Biol. **140**, 1407 (1998).
[12] M. Thormahlen, A. Marx, S. A. Müller, Y.-H. Song, E.-M. Mandelkow, U. Aebi, and E. Mandelkow, J. Mol. Biol. **275**, 795 (1998).
[13] H. Salman, A. Abu-Arish, S. Oliel, A. Loyter, J. Klafter, R. Granek, and M. Elbaum, Biophys. J. **89**, 2134 (2005).
[14] J. D. Lane and V. J. Allan, Mol. Biol. Cell **10**, 1909 (1999).
[15] J. Gelles, B. J. Schnapp, and M. P. Sheetz, Nature (London) **331**, 450 (1988).
[16] A. Caspi, R. Granek, and M. Elbaum, Phys. Rev. Lett. **85**, 5655 (2000).
[17] A. Caspi, R. Granek, and M. Elbaum, Phys. Rev. E **66**, 011916 (2002).
[18] K. Svoboda, C. F. Schmidt, B. J. Schnapp, and S. M. Block, Nature (London) **365**, 721 (1993).
[19] K. Svoboda, P. P. Mitra, and S. M. Block, Proc. Natl. Acad. Sci. U.S.A. **91**, 11782 (1994).
[20] Y. Inoue, Y. Y. Toyoshima, A. H. Iwane, S. Morimoto, H. Higuchi, and T. Yanagida, Proc. Natl. Acad. Sci. U.S.A. **94**, 7275 (1997).
[21] R. Simmons, Curr. Biol. **6**, 392 (1996).
[22] M. Tomishige and R. D. Vale, J. Cell Biol. **151**, 1081 (2000).
[23] A. Reilein, S. Yamada, and W. J. Nelson, J. Cell Biol. **171**, 845 (2005).
[24] G. Zumofen, J. Klafter, and A. Blumen, Phys. Rev. A **42**, 4601 (1990).
[25] A. Ajdari, Europhys. Lett. **31**, 69 (1995).
[26] S. Redner, Phys. Rev. E **56**, 4967 (1997).
[27] J. Honkonen, J. Phys. A **24**, L1235 (1991).
[28] R. Lipowsky, S. Klumpp, and T. M. Nieuwenhuizen, Phys. Rev. Lett. **87**, 108101 (2001).
[29] T. M. Nieuwenhuizen, S. Klumpp, and R. Lipowsky, Europhys. Lett. **58**, 468 (2002).
[30] By the word "efficiency" we do *not* refer to the efficiency of a motor protein in transforming chemical energy into work.
[31] G. Matheron and G. de Marsily, Water Resour. Res. **16**, 901 (1980).
[32] A. Georges, J.-P. Bouchaud, and P. Le Doussal, J. Phys. (Paris) **48**, 1855 (1987).